# Redundant Crossfire: A Technique to Achieve Super-Resolution in Neurostimulator Design by Exploiting Transistor Mismatch

Anh Tuan Nguyen<sup>®</sup>, *Member, IEEE*, Jian Xu<sup>®</sup>, *Member, IEEE*, Diu Khue Luu<sup>®</sup>, Cynthia K. Overstreet, Jonathan Cheng<sup>®</sup>, Edward W. Keefer, and Zhi Yang, *Member, IEEE* 

Abstract—A high-resolution neurostimulator is the essential component of many bidirectional neural interfaces. In practice, the effective resolution of fully integrated neurostimulator designs is often hindered by the transistor mismatch, especially in submicrometer CMOS processes. In this article, we present a new circuit technique called redundant crossfire (RXF) to address this challenge. It is derived from our redundant sensing (RS) framework, which aims at engineering information redundancy into the system architecture to enhance its effective resolution. RXF involves combining (i.e., crossfiring) the outputs of two or more current drivers to form a redundant structure that, when properly configured, can produce accurate current pulses with an effective super-resolution beyond the limitation commonly permitted by the physical constraints. Unlike any previous works, the proposed technique achieves high-accuracy by directly exploiting the random transistor mismatch with an excessively large mismatch ratio of 10%-20%. The effectiveness of RXF is verified through both Monte Carlo simulations and measurement results of a fully integrated neurostimulator chip. Equipped with a 5-bit current digital-to-analog converter (IDAC) and two 4-bit current multipliers, the stimulator achieves an effective resolution of 9.75 bits in a 1.1-mA full range. An application of the fabricated chip is to deliver neuro-feedback to a human amputee through peripheral nerves where the amplitude of stimulation pulses is accurately controlled to encode the tactile response's intensity.

Index Terms—Bidirectional neural interface, high-resolution, human—machine interface, neurostimulator, neuro-feedback, neuroprosthesis, redundant crossfire (RXF), redundant sensing (RS), super-resolution, transistor mismatch.

Manuscript received August 21, 2020; revised November 12, 2020 and December 28, 2020; accepted January 27, 2021. Date of publication February 17, 2021; date of current version July 23, 2021. This article was approved by Associate Editor Nick van Helleputte. This work was supported in part by the Defense Advanced Research Projects Agency (DARPA) under Grant HR0011-17-2-0060 and Grant N66001-15-C-4016, in part by internal funding from the University of Minnesota, in part by NIH under Grant R21-NS111214, in part by the NSF CAREER under Award 1845709, and in part by Fasikl Inc. (Corresponding author: Zhi Yang.)

Anh Tuan Nguyen and Zhi Yang are with the Department of Biomedical Engineering, University of Minnesota, Minneapolis, MN 55455 USA, and also with Fasikl Inc., Minneapolis, MN 55113 USA (e-mail: yang5029@umn.edu). Jian Xu and Diu Khue Luu are with the Department of Biomedical

Engineering, University of Minnesota, Minneapolis, MN 55455 USA.

Cynthia K. Overstreet is with Nerves Inc., Dallas, TX 75214 USA. Jonathan Cheng is with the Department of Plastic Surgery, University of Texas Southwestern Medical Center, Dallas, TX 75390 USA.

Edward W. Keefer is with Nerves Inc., Dallas, TX 75214 USA, and also with Fasikl Inc., Minneapolis, MN 55113 USA.

Color versions of one or more figures in this article are available at https://doi.org/10.1109/JSSC.2021.3057041.

Digital Object Identifier 10.1109/JSSC.2021.3057041

# I. INTRODUCTION

ELECTRICAL neurostimulation is a well-established method for interfacing with neural circuits. Proper uses of neurostimulation could offer a viable conduit to relay information to the human mind, which is widely used in neuroprosthesis applications to augment or replace human senses' missing function. They include retinal implants [1]–[5] for restoring vision, cochlear implants [6], [7] for restoring audition, prosthetic limbs [8]–[15] for restoring somatosensation, and so on. At the heart of those implantable or wearable devices are fully integrated neurostimulators which function is to generate stimulation pulses with accurately controlled parameters such as pulsewidth, current amplitude, and frequency [16]–[23].

Like any analog integrated circuit (IC), it is challenging to implement a high-resolution neurostimulator without incurring penalties such as large silicon area and/or high power consumption because of the mismatch error. Studies have shown that the random mismatch error is one of the major factors limiting the design's effective resolution [24], [25], especially when scaling down the circuits to submicrometer CMOS processes [26], [27]. Arising from random variations in the lithography process and beyond the designers' control, mismatch error is the scourge of high-resolution analog IC designs [34]. Nearly, all neurostimulator designs are affected because mismatches appear in any type of components, such as transistors, diodes, resistors, and capacitors. Current-controlled stimulators (CCSs) like this work and [1]-[5], [16]-[19] are mostly affected by transistor mismatches, while voltage-controlled stimulators (VCS) [38], [39] and switched-capacitor stimulators (SCS) [35]–[37] are mostly affected by transistor and capacitor mismatches. Mismatches influence the circuit's ability to produce accurate current/voltage output and match the negative and positive stimulation phases leading to charge imbalance issues. Compensating for these errors requires extra calibration circuits that add complexity, area, and power.

Here, we present an entirely different approach to address this challenge, not by avoiding or compensating the mismatch error but by embracing and exploiting excessively large mismatches to achieve super-resolution over tenfold beyond the intrinsic resolution of the design. The proposed circuit technique is called redundant crossfire (RXF), which

0018-9200 © 2021 IEEE. Personal use is permitted, but republication/redistribution requires IEEE permission. See https://www.ieee.org/publications/rights/index.html for more information.

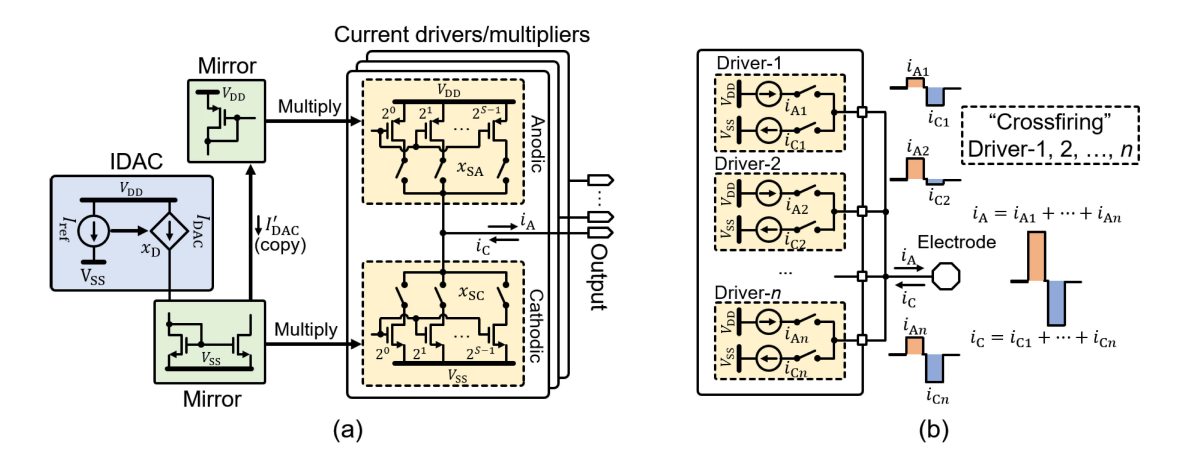


Fig. 1. (a) Conceptual design of a standard biphasic stimulator where several current drivers with a low-resolution multiplying factor share a IDAC. (b) Proposed RXF technique involves combining and synchronizing (i.e., "crossfiring") the output of two or more drivers. Each driver contributes a small amount of current to generate the final stimulation pulse.

involves combining (i.e., crossfiring) the output of two or more current drivers to form a redundant structure. In the presence of large random mismatch errors (10%–20%), such redundant structure can be configured to generate the output with an effective resolution that is many times above the Shannon limit determined by the physical constraints like the number of unit-transistors. RXF is a practical derivation of our theoretical framework, including redundant sensing (RS) [28], [29] and RS-based super-resolution [30], where information redundancy is elegantly engineered and manipulated to boost the system resolution. Furthermore, by handling extremely large mismatches, the proposed technique opens up possibilities for implementing high-resolution analog circuits in deep submicrometer technology.

To demonstrate the effectiveness of RXF, we design a neurostimulator chip where each current driver has only a 5-bit current digital-to-analog converter (IDAC) and two 4-bit current multipliers. By crossfiring two drivers, it is feasible to achieve an effective resolution of 9.75 bits or  $27 \times$  the ideal intrinsic resolution of each IDAC. The performance boost is verified through benchtop measurements of fabricated chips and consistent with the Monte Carlo simulations, suggesting that the proposed technique is robust and dependable. Finally, we show an example using the prototype chip in a neuroprosthesis application to restore somatosensation by accurately modulating the stimulation pulses' current amplitude.

#### II. PRINCIPLES OF OPERATION

## A. RXF

The key to achieving high-resolution with RS is to create a structure of information redundancy where numerous different internal configurations can represent the same output. In practice, such a structure must be realized without using excessive

<sup>1</sup>Combining 5-bit IDAC and two 4-bit multipliers does not give 9-bit output. For example, 37, 41, 43, . . . cannot be expressed as a multiple of two numbers less than 31. A 5-bit IDAC and two 4-bit multipliers only have a total of 64 unit transistors. A conventional 10-bit system generally needs 1024 unit transistors.

physical resources. Here, we show a simple yet effective way to form the needed redundancy with a subtle modification of the conventional circuit.

Fig. 1(a) shows the conceptual design of a standard biphasic, current-mode stimulator which consists of a IDAC, current mirror circuits, and anodic (positive) and cathodic (negative) output current drivers/multipliers. The drivers perform dual functions: scaling the IDAC current by a multiplying factor and driving the constant current to the electrode. In each channel, there is one IDAC that is shared among several different drivers. Subsequently, the anodic  $i_A$  and the cathodic  $i_C$  output current are as follows:

$$i_A = I_{\text{IDAC}} \cdot x_{\text{SA}} = I_{\text{ref}} \cdot x_D \cdot x_{\text{SA}}$$
  
 $i_C = I_{\text{IDAC}} \cdot x_{\text{SC}} = I_{\text{ref}} \cdot x_D \cdot x_{\text{SC}}$  (1)

where  $I_{\text{ref}}$  is a fixed reference current,  $(x_{\text{SA}}, x_{\text{SC}})$  are the multiplier codes, and  $x_D$  is the IDAC code.

Fig. 1(b) shows an RXF structure that is created by combining or "crossfiring" the output of two or more drivers. Each driver contributes a small amount of current, which can be independently adjusted to generate the final stimulation pulse. The timing of the pulses produced by different drivers must be synchronized, i.e., the anodic and cathodic currents are turned on/off at exact moments such that they behave like a single stimulation channel. This can be easily achieved with an on-chip timing generator.

The RXF structure is redundant because a similar output code can be generated by numerous different configurations of the IDAC and multiplier. Fig. 2(a) shows the examples of several circuit configurations that produce the same theoretical output when there is no mismatch error. Here, the IDAC's resolution is  $N_{\rm D}=5$  and the multiplier's resolution is  $N_{\rm S}=4$ . Both four configurations of different IDAC and multiplier values generate the same output code  $i_{\rm C}=8$ . In practice, there are tens to hundreds of distinct configurations associated with each output code. They have complex mutual relationships that depend on the resolution of the IDAC, multiplier, and the number of crossfire drivers.

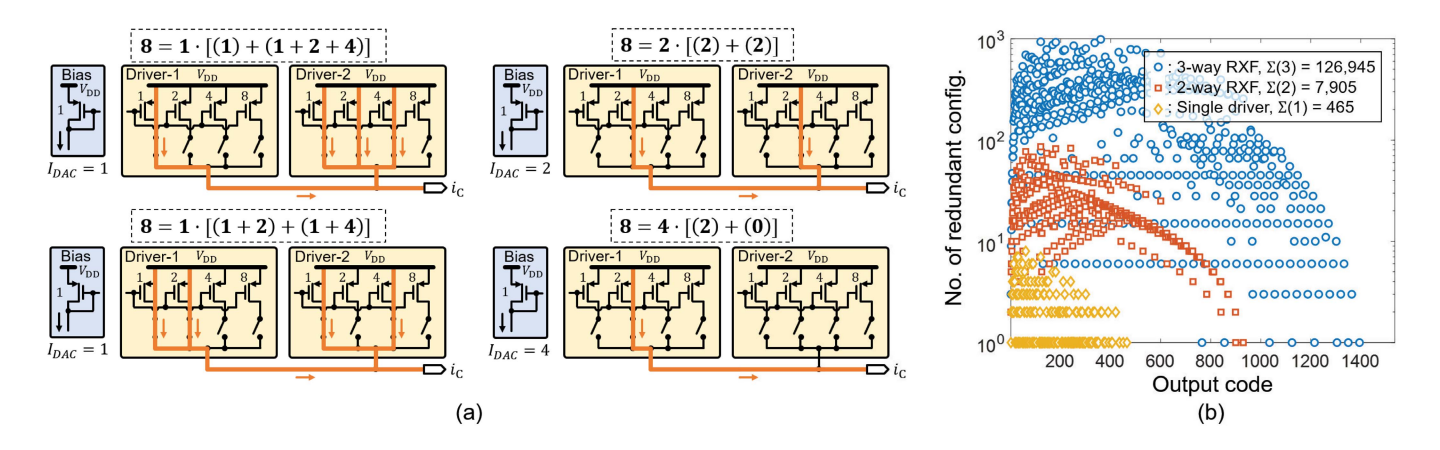


Fig. 2. Crossfiring two or more drivers effectively create a redundant structure where a similar output can be generated by numerous different configurations of the IDAC and multiplier. (a) Examples of several circuit configurations that produce the same theoretical output with no mismatch. (b) Distribution of the number of redundant configurations corresponding to each output code in a single driver, a two-way RXF structure, and a three-way RXF structure ( $N_D = 5$  and  $N_S = 4$ ).

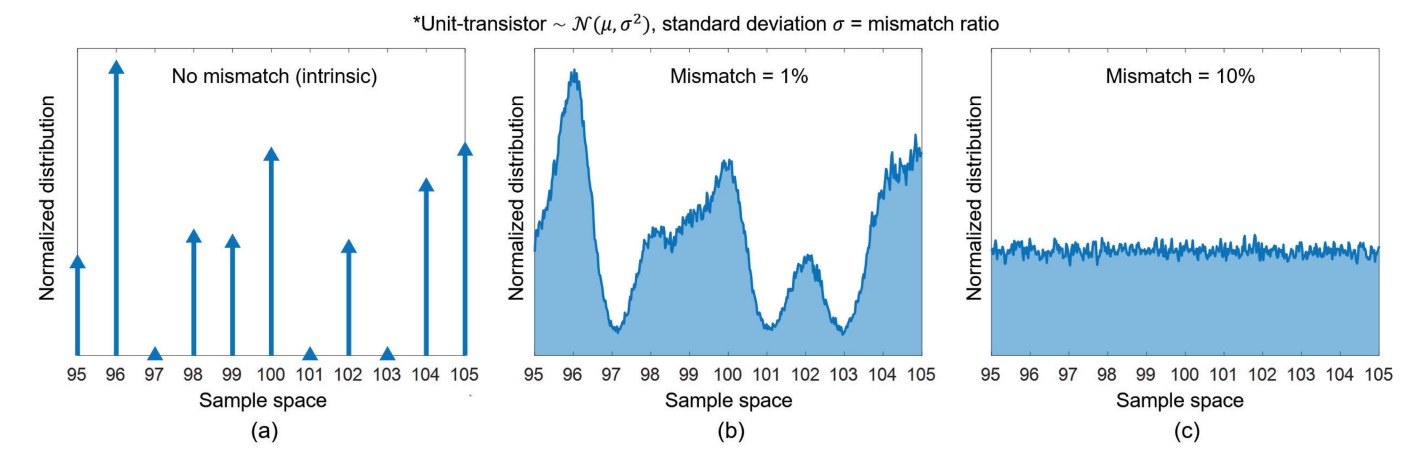


Fig. 3. "Code diffusion" is a unique property of an RS structure that enables super-resolution. (a) When there is no mismatch, redundant configurations generate the exact same analog output. (b) With random mismatch error, the actual values of different outputs begin to deviate from their original states and "diffuse" into the adjacent sample space. (c) With large mismatch error, their values distribute evenly across the sample space and allow generating sub-integer codes (super-resolution) that are not normally possible.

The total number of non-zero, distinct configurations in a n-way RXF structure with n crossfire drivers is as follows:

$$\Sigma(n) = (2^{N_{\rm D}} - 1) \cdot [(2^{N_{\rm S}})^n - 1]. \tag{2}$$

With each additional crossfire driver, the physical resources (i.e., chip area) increase linearly, while the number of configurations (i.e., level of redundancy) grows exponentially. Fig. 2(b) shows the distribution of the number of redundant configurations corresponding to each output code in a single driver, two-way RXF, and three-way RXF structure ( $N_D = 5$ ,  $N_S = 4$ ) across the sample space. Additional crossfire drivers extend the max output and exponentially increase the level of redundancy, which is essential to achieve super-resolution.

## B. Super-Resolution

Our previous work Luu and Nguyen *et al.* [30] layouts the theoretical foundation of RS-based super-resolution. Super-resolution is enabled by a unique property of the RS architecture called "code diffusion." Fig. 3 shows the

distribution<sup>2</sup> of the analog outputs produced by different configurations of a two-way RXF structure ( $N_D = 5$  and  $N_{\rm S}=4$ ). The analog outputs are contained in a continuous sample space with values ranging from 0 to a maximum value of approximately  $31 \cdot (15+15) = 930 \text{ LSB}$ , where  $1\text{LSB} = I_{\text{ref}}$ . To model the random mismatch error, we assume that each unit transistor of both the IDAC and multipliers has a Gaussian distribution; and the standard deviation is the mismatch ratio. When generating random samples, negative values are set to zero. Fig. 3(a) shows that, with no mismatch errors, redundant configurations generate the exact same analog outputs that are centered at integer codes [0, 1, 2, 3, ...]. Their distributions are represented by Dirac delta impulses with the weight equal to the number of configurations. Fig. 3(b) shows that, with small random mismatch errors, the actual values of different analog outputs begin to deviate from their original states and "diffuse" into the adjacent sample space. Fig. 3(c) shows that,

<sup>2</sup>The distributions in Fig. 3(b) and (c) are computed using kernel density estimation with a bandwidth h = 0.01, number of random samples N = 1000.

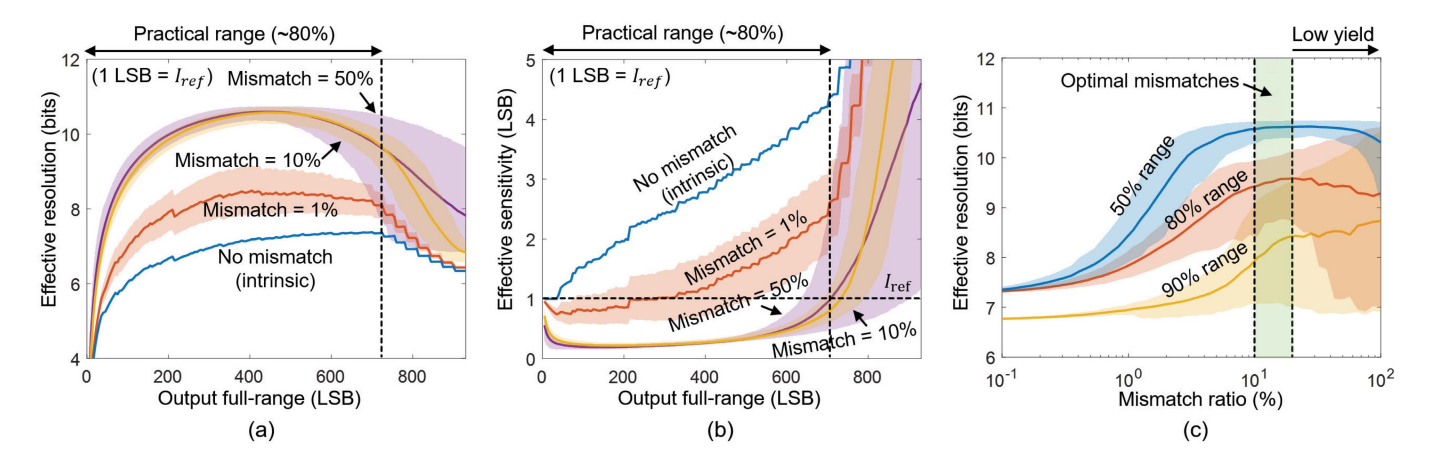


Fig. 4. Monte Carlo simulations (N = 1000) show substantial resolution enhancement can be achieved using a two-way RXF structure with low-resolution IDAC and multiplier ( $N_D = 5$ ,  $N_S = 4$ ). (a) Effective resolution and (b) effective sensitivity are calculated for each value of the output full range. At a practical full range of about 80% of the maximum output code, RXF enables super-resolution with 2–3 bits beyond the intrinsic baseline. (c) Effective resolution at different output full range versus mismatch ratio shows a 10%–20% mismatch could be optimal. (Shaded error band = 90% confidential interval.)

with large mismatch errors, the analog output values distribute evenly across the sample space.

Code diffusion allows generating sub-integer codes [0.1, 0.2, 0.3,...] with a certain probability that are not normally possible. These sub-integer codes correspond to the sample space's finer partition, and thus, an effective super-resolution beyond the baseline figure. For example, to achieve (+1) super-resolution, redundant configurations that generate all the sub-integer codes [0, 0.5, 1, 1.5,...] must be found. To achieve (+2) super-resolution, the required sub-integer codes are [0, 0.25, 0.5, 0.75, 1,...]. While identifying the correct configuration for every output code is an NP-hard optimization problem, it is only possible in an information redundant architecture such as RS. The probability of accomplishing this task is maximized when the codes distribute evenly across the sample space, as shown in Fig. 3(c).

Monte Carlo simulations are used to evaluate the theoretical super-resolution that can be achieved with the proposed method. Fig. 4 shows the simulation results (N=1000) where even a two-way RXF structure with low-resolution IDAC and multiplier ( $N_{\rm D}=5$  and  $N_{\rm S}=4$ ) is sufficient to facilitate a substantial enhancement. Here, the mismatch error is applied to elements of both the IDAC and multiplier equally. In each simulation, the RXF structure is optimized by a brute-force approach, i.e., sorting through all the redundant configurations, and finds ones that generate the desired output with the least amount of error.

We use the "effective resolution" and "effective sensitivity" to measure quantitative performance. The "effective resolution" is defined as the "Shannon entropy" [28], [30], which is computed with respect to a targeted resolution (12 bits) as follows:

$$M_{N_x} = \sum_{d=0}^{2^{N_x} - 1} \int_{\theta_d}^{\theta_{d+1}} \left( x_A - \frac{d+0.5}{2^{N_x}} \right)^2 dx_A$$

$$H_{N_x} = -\log_2 \sqrt{12 \cdot M_{N_x}}$$
(3)

where  $H_{N_x}$  is the effective resolution (entropy) with respect to the targeted resolution  $N_x$ ,  $M_{N_x}$  is the normalized total mean

square error integrated over each digital code  $d \in [0, 2^{N_x} - 1]$ , and  $\theta_0, \theta_1, \ldots$  are the corresponding analog outputs. The targeted resolution  $N_x$  is the reference upper bound of the device's super-resolution, which is arbitrarily defined over the full range. No matter how high the targeted resolution is defined, the effective resolution  $H_{N_x}$  would converge to a maximum value. The "effective sensitivity" is defined as the smallest change in output current that could be accurately produced by the device. It is computed as follows:

$$S_{N_x} = I_{\text{ref}} \cdot FR/2^{H_{N_x}} \tag{4}$$

where  $S_{N_x}$  is the effective sensitivity and FR is the targeted output full range. The metrics are evaluated for all values of the full range from 0 to the maximum value of 930 LSB.

Effective resolution and sensitivity presented in Fig. 4(a) and (b) are highly correlated with the number of redundant configurations shown in Fig. 2(b) (two-way RXF). The effective resolution in the first 0–50 LSB is low because there are not enough redundant configurations. It reaches the highest point at approximately 50%–80% (450–750 LSB) of the maximum full range where most of the redundant configurations are located. At the practical full range of 80% (750 LSB), the RXF structure achieves 2–3 bits super-resolution beyond the intrinsic baseline. The intrinsic baseline is the best resolution that can be attained with the conventional structure and zero mismatches. Beyond this point, the resolution drops rapidly because the redundant configurations become sparsely distributed and, thus, insufficient redundancy.

The results of Fig. 4 clearly demonstrate a unique and fundamental property of the proposed method: mismatch error is utilized to enhance resolution. Unlike any previous design in the literature, the proposed system becomes more accurate when the mismatch ratio *increases* from 0% to 10%. This is because a larger mismatch error leads to a more even distribution of redundant values across the sample space (see Fig. 3), which maximizes the probability of finding a configuration to generate the desired output. The effectiveness also becomes more consistent (i.e., smaller deviation) when the mismatch ratio *increases* from 0% to 10%. This implies super-resolution

is high-yield, replicable, and does not rely on a specific random configuration.

The simulations also indicate that an extreme mismatch ratio may not be beneficial nor realistic, and a 10%–20% mismatch could be the optimal range. Fig. 4(a) and (b) shows that, at 50% mismatch ratio, not only there is no significant additional boost to the effective resolution but also the deviation starts to widen. This suggests a lower yield as fewer samples could achieve the desired super-resolution, and the structure becomes unreliable. Fig. 4(c) shows the effective resolution computed at 50%–80%–90% range with different mismatch ratio from 0.1% to 100%. A mismatch ratio within 10%–20% yields the optimal super-resolution at most ranges. Beyond 20% mismatch, the deviation rapidly increases, lowering the yield.

Nevertheless, the presented simulation results should only serve as a design guideline. As a rule of thumb, we use the Gaussian distribution as the random mismatch error model because of the central limit theorem. This is a rather simplistic assumption as the real-life transistor mismatch could be far more complex and difficult to be quantified. Mismatch error could affect multiple aspects of the device such as size (W/L), threshold voltage, intrinsic gain, and so on, depending on the operating conditions such as supply voltage, bias current, corners, and temperature. Thus, an actual VLSI implementation presented in Section III is still the most accurate way to validate the proposed technique.

#### C. Conventional Redundancy Versus RS

Our RS-based super-resolution technique is distinct from any previous utilization of redundancy in conventional designs [28], [29].

The most common use of redundancy in conventional systems is *temporal redundancy* or oversampling. It involves using the same structure to sample the output numerous times; each produces a slightly different outcome due to noise, offset, and so on. The final result is obtained by averaging or integrating these redundant samples. To achieve a significant resolution enhancement, the output must be sampled at a much higher rate than the Nyquist frequency, which consumes a proportional amount of energy and bandwidth. Temporal redundancy is widely used in IC designs (e.g.,  $\Delta\Sigma$  architecture) and other applications (e.g., oscilloscope) to enhance the effective resolution with the existing hardware.

Another use of redundancy in conventional systems is *physical redundancy*. It involves using redundant structures to sample the same output, then averaging or integrating the results. These redundant structures could be physically separated instances of the same actuator/sensor or independent datapaths in the actuator/sensor's internal architecture. Physical redundancy is resource-intensive and thus is not a prominent approach to enhance resolution. Most uses of physical redundancy are limited to 2–3 times redundancy and primarily aim for fault-tolerance.

The proposed RS-based technique utilizes *information* redundancy. It involves designing the actuator/sensor's architecture such that numerous distinct internal configurations can

produce each output. By selecting the optimal subset of these redundant configurations, significant resolution enhancement [28], [31] or super-resolution [30] can be achieved. With RS, an excessive level of information redundancy, hundreds to thousands of times the conventional approach, could be incorporated into the actuator/sensor without any addition of energy, bandwidth, or physical resources. This is not possible with conventional designs, which are *information orthogonal*, i.e., each input corresponds to a unique outcome. The drawback of information redundancy is that the structure must be optimized, which is an NP-hard problem. Fortunately, in certain cases, it only needs to be done once, as shown here in a neurostimulator design.

## III. FULLY INTEGRATED NEUROSTIMULATOR

#### A. Circuit Implementation

Fig. 5(a) shows the schematic of a fully integrated neurostimulator design with two-way RXF architecture  $(n=2,N_{\rm D}=5,$  and  $N_{\rm S}=4)$ . The circuit shares basic functional blocks with our previous work [21], which is mainly based on the op-amp-assisted boosted-cascode current driver and current mirror. Here, the design trades off area to achieve ultra-high output impedance. The estimated output impedances are >1 G $\Omega$  at 1 mA (source) and >50 G $\Omega$  at -1 mA (sink). The output voltage range is set by  $V_{\rm DN}=V_{\rm SS}+0.5$  and  $V_{\rm DP}=V_{\rm DD}-0.5$ , which results in a compliance of  $\pm 4.5$  V. The reference current is generated by a voltage-to-current converter circuit, and the value is set to  $I_{\rm ref}=1.5~\mu{\rm A}$  by  $V_{\rm DD}$  and an external resistor.

Contrary to conventional wisdom, a large level of transistor mismatch is desirable in this design. The implication is that RS-based structures would work better in a deep submicrometer process with a large amount of mismatch. The proposed technique's key advantage is to remove the concern on mismatch error, allowing the designers to utilize smaller sized components or relax the layout constraints, which are often needed to suppress mismatches in past designs. However, in situations where "naturally" occurring mismatch is thought to be insufficient, it is possible to increase the amount of error purposely. Fig. 5(b) shows the Monte Carlo simulations (N = 100) of the output current when selecting 1 bit of the IDAC. The random error (spread) is caused by variations and mismatches, while the systematic error (offset) is caused by non-ideal schematic and parasitics. If the random error does not reach the desired level (e.g., 10%–20%), "artificial" mismatches could be created by arbitrarily tuning the individual unit transistors' size (W/L) by tens to a few hundred nanometers from the nominal value. The tuning values are randomly generated in a computer and manually added to each unit transistor, which would influence the systematic error, as shown in Fig. 5(b). The procedure is repeated with each bit of the IDAC and multiplier if necessary. It is ideally done with post-layout simulations because the parasitics could bring additional systematic errors.

Table I shows the W/L dimensions of key transistors and transistor arrays highlighted in Fig. 5(a). Minimum feature-size transistors are used whenever possible

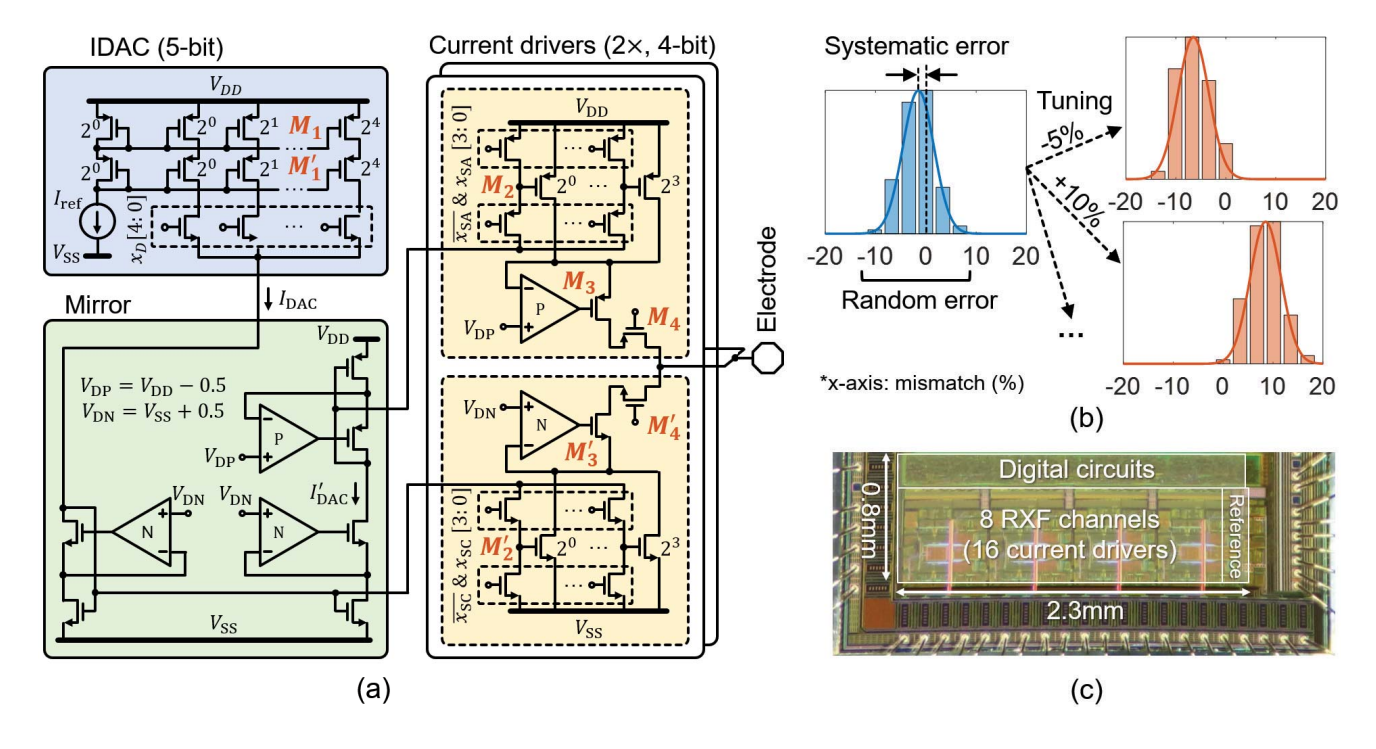


Fig. 5. (a) Circuit implementation of a neurostimulator design with two-way RXF architecture (n = 2,  $N_D = 5$  and  $N_S = 4$ ). (b) "Artificial" mismatches could be created by tuning individual unit transistor if the level of "natural" random mismatches is not sufficient. (c) Micrograph of the fully integrated neurostimulator with eight RXF channels (16 current drivers).

TABLE I
DIMENSIONS OF HIGH-VOLTAGE LDMOS

IDAC (5-bit)	$M_1, M_1'$	PMOS: 64× (4.0/0.5 μm) (minimum size)		
Drivers (4-bit)	$M_2$	PMOS: 16× (32.0/1.0 μm)		
	$M_2'$	PMOS: 16× (16.0/1.0 μm)		
Cascode	$M_3$	PMOS: 32× (8.0/0.5 μm)		
	$M_3'$	NMOS: 8× (8.0/0.7 μm)		
Output switches	$M_4$	PMOS: 8× (10.0/0.5 μm)		
	$M_4'$	NMOS: 8× (8.0/0.7 μm)		

(e.g., IDAC) to maximize the mismatch error. Nevertheless, larger transistors are needed for the driver, cascode, and output switches to meet the voltage-drop requirement for output compliance. The anodic circuits generally use larger transistors than the cathodic counterparts because the current drivability of PMOS is about 50% less than that of NMOS.

The chip is fabricated in the GlobalFoundries 0.18- $\mu$ m BCDLite process. We use isolated high-voltage LDMOS transistors, which could support up to 30 V. The micrograph of the chip is shown in Fig. 5(c), which contains eight RXF channels (16 current drivers) and occupies a core area of 0.8 mm  $\times$  2.3 mm. The chip's overall static power consumption is approximately 2.4 mW for the analog circuits at 10-V ( $\pm$ 5 V) supply and 1.6 mW for the digital circuits at 1.8-V supply.

Most static power is from the high-voltage op-amps' bias current, which can be shut down while a channel is not in use

Table II shows the specifications of the proposed neurostimulator in comparison with other state of the arts. It is worth noting that the specifications, such as voltage compliance, current range, and current resolution, highly depend on the specific application and electrode impedance. Our stimulator is particularly developed toward implantable peripheral nerve applications using cuff and intrafascicular microelectrodes [32]. This requires a compliance voltage of 10 V and a max current of about 1 mA, which have been found to be sufficient in our previous clinical trials using commercial benchtop stimulators [33]. The design primarily focuses on achieving high-resolution output, both current amplitude and timing. Furthermore, we report the effective resolution measured at the output, while other works only provide the baseline resolution, which could be up to 1 bit lower in practice due to mismatch error.

# B. Digital Controller and Optimization

Fig. 6(a) and (b) shows the proposed stimulator's control strategy, which consists of both on-chip and off-chip logic/memory. To achieve super-resolution, an RXF structure must be optimized. This is done with a one-time factory calibration procedure where all the driver's output currents are measured. There are  $2 \cdot (2^5 - 1) \cdot (2^4 - 1) = 930$  non-zero values per driver to be measured, both anodic and cathodic. All the crossfire configurations are then computed. There are  $2 \cdot (2^5 - 1) \cdot (2^4 \cdot 2^4 - 1) = 15\,810$  non-zero configurations

	Lo et al. '16 [2]	Lee et al. '18 [18]	Rozgić et al. '18 [17]	Zhou et al. '19 [19]	This work
Process	0.18μm HV CMOS	0.13μm CMOS	0.18μm HV CMOS	0.18μm HV CMOS	0.18µm BCDLite
No. of channels*	40	4	8	4	8
Area per channel (mm²)	0.19	0.20	0.80	0.15	0.23
Max current (mA)	0.5	1.86	5.1	5.0	1.10
Current precision (µA)	10	60	20	20	1.28
Resolution** (bits)	7**	5**	8**	8**	9.75
Supply (V)	24	4	10	12	10
Pulse-width (msec)	0.01 - 8	0.095 - 0.304	0.01	0.015 - 0.5	0.01 - 6.56
Timing precision (µsec)	10	9.5	10	15.6	0.1
Charge balancing	Passive discharge	Post-stimulation short pulses	Passive discharge	Current source reuse, 0.016%	RXF coarse & fine, < 0.005%
Application	Spinal cord	Peripheral nerve	Cortical	Cortical	Peripheral nerve

TABLE II
SPECIFICATIONS OF THE PROPOSED NEUROSTIMULATOR IN COMPARISON WITH OTHER STATE OF THE ARTS

<sup>\*\*</sup> For other works, the baseline resolution is reported. The effective resolution due to mismatch could be up to 1-bit lower.

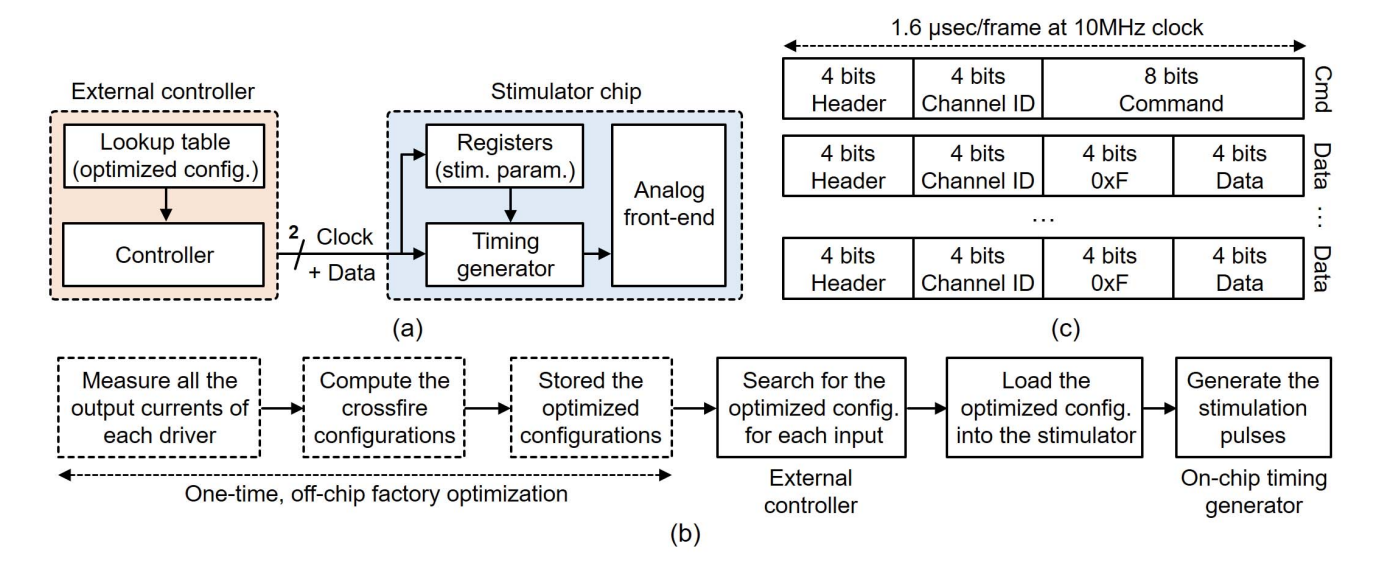


Fig. 6. (a) and (b) Control strategy of the proposed stimulator consisting of on-chip and off-chip components. To achieve super-resolution, the RXF structure must be optimized by a one-time factory optimization procedure. The optimized configurations are stored on an external lookup table. (c) Data frame of the customized transmission protocol.

per channel in a two-way RXF structure. The optimized configuration associated with each desirable output currents can be easily found by sorting through all the available values in a brute-force manner. While it is not an elegant solution, the optimization procedure only needs to be done once with off-chip computation. The optimized configurations are then stored in an external lookup table. With a 10-bit effective resolution, the table size would be  $2 \cdot 2^{10} \cdot (5 + 4 + 4) = 26\,624$  bits (3.3 kB) per channel.

An external controller maps each desirable output with the lookup table's optimized configuration during normal operation. The configuration is loaded into the stimulator chip via a customized two-wire transmission protocol consisting of a 10-MHz clock line and a data line. Fig. 6(c) shows the protocol's 16-bit frames. The first 4 bit is the sync header, whose value rotates in  $0\times0-0\times F$ . If the header is out of sync, the stimulator chip would immediately reset, and all the outputs are turned off. This prevents runaway stimulation when the transmission is disrupted. The second 4 bit is the channel ID. The last 8 bit is either the command or a  $(0\times F)$  mask with a 4-bit data nibble. Each transmission starts with a "command" frame followed by several "data" frames. There are 240 possible commands  $(0\times00-0\times EF)$  that govern every function of the stimulator. The number of data frames varies

<sup>\*</sup> Independent channels or current drivers without multiplexing.

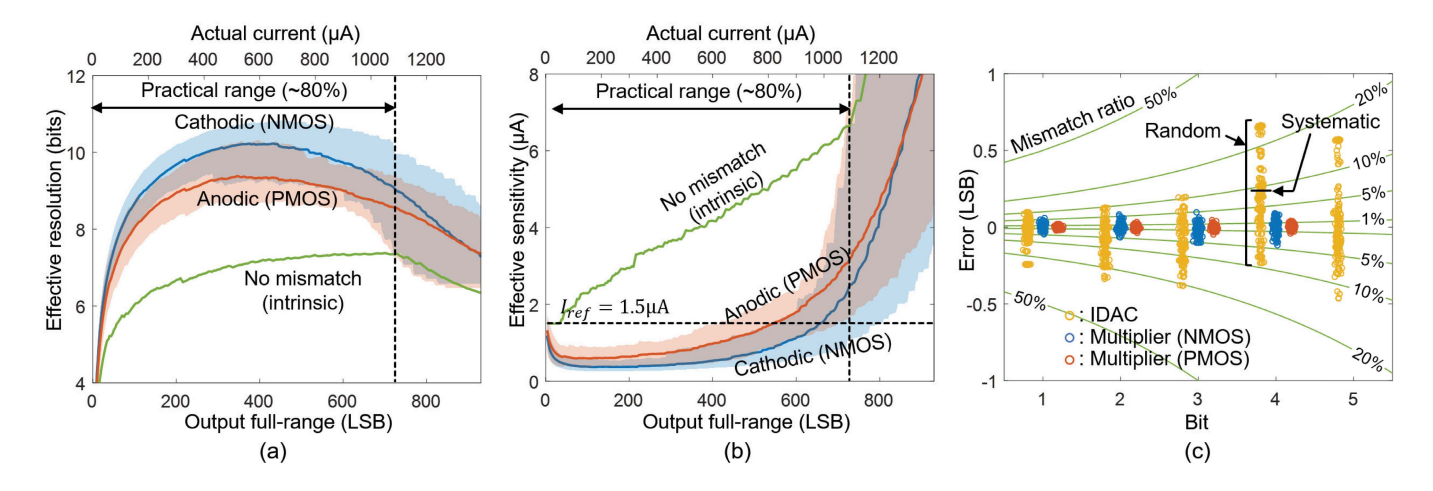


Fig. 7. Measurement results ( $N_{\rm Ch} = 8$  and  $N_{\rm IC} = 10$ ) of (a) effective resolution and (b) effective sensitivity show substantial enhancement (2–3 bits) from the intrinsic baseline. The data are relatively consistent with the theoretical prediction presented in Fig. 4 over the same output full range with a reference current  $I_{\rm ref} = 1.5 \ \mu \rm A$ . (c) Mismatch error of each bit of the IDAC and multiplier computed from the measured current outputs. The NMOS has a larger spread than PMOS, explaining the cathodic drivers (NMOS) are more accurate than anodic drivers (PMOS). Shaded error band = 90% confidential interval.

depending on the specific command, e.g., setting the IDAC (5 bit) requires two data frames while generating that the stimulation pulse does not require any data. At a data rate of 10 Mb/s, the frame time is 1.6  $\mu$ s/frame.

The on-chip timing generator circuits produce the stimulation pulses. This is essential to achieve a near-perfect synchronization of multiple drivers in a crossfire formation. All the stimulation parameters, such as pulsewidth, IDAC, multiplier, and polarity, are stored in integrated registers. The anodic and cathodic phases of a biphasic pulse can be independently configured to produce both symmetrical and asymmetrical stimulation with any ratio setting. New IDAC and multiplier configurations are loaded during the interphase delay. We use a 16-bit register at a base clock of 10 MHz to control the pulsewidth. This allows generating any timing from 0.01 to 6.56 ms with 0.1- $\mu$ s adjustment step. The adjustment step is also used to digitally compensate for the residual mismatch between the anodic and cathodic currents to ensure charge balancing. This is achieved by tuning the anodic and cathodic pulsewidth such that

$$\min |i_A \cdot (t_A + \Delta t_A) - i_C \cdot (t_C + \Delta t_C)|. \tag{5}$$

The adjustment timings ( $\Delta t_A$  and  $\Delta t_C$ ) are computed by the external controller based on the measured currents ( $i_A$  and  $i_C$ ) and required pulsewidth ( $t_A$  and  $t_C$ ).

# C. Measurement Results

Fig. 7(a) and (b) shows the measurement results of the effective resolution and effective sensitivity. The data are acquired from different channels and chips ( $N_{\rm Ch}=8$  and  $N_{\rm IC}=10$ ). The reference current is set to  $I_{\rm ref}=1.5~\mu{\rm A}$ , which translates to a practical output full range of approximately 1.1 mA. The proposed RXF technique results in an effective super-resolution of 2–3 bits beyond the intrinsic baseline, conforming with the theoretical analysis. The effective sensitivity is well below the reference current across most of the output full range, which would be impossible in any

previous work. Fig. 7(c) shows the actual mismatch error computed from the measured current outputs for each bit of the IDAC and multiplier. The IDAC exhibits desirable random and systematic error, falling within the optimal 10%–20% range. However, the current multiplier's mismatch is insufficient. The NMOS has a larger spread than PMOS, explaining the results in Fig. 7(a) and (b) where the cathodic drivers (NMOS) have higher effective resolution than the anodic drivers (PMOS). Nevertheless, additional "artificial" mismatches need to be added to the multiplier's unit transistors in future revisions of the chip.

Fig. 8 shows the measured integral nonlinearity (INL) and differential nonlinearity (DNL) of a stimulator channel. Here, both the x-axis and y-axis are normalized to the targeted resolution of 12 bits over the 1.1-mA full range. The codes are optimized so that the outputs are always monotonic. The measured channel achieves an effective super-resolution of 9.75 bits and effective sensitivity of 1.28  $\mu$ A. Unlike a conventional ADC/DAC, the INL and DNL of an RXF device are not symmetrical. Lower digital codes are more accurate because they contain more redundant configurations. The large spikes of INL/DNL data in higher digital codes (3500–4000 LSB) and the brief peak in 0–50 LSB are associated with regions where there are not enough redundant configurations and their distribution are sparse, as shown in Fig. 2(c).

Fig. 9(a) shows the examples of the measured output current with a  $1-k\Omega$  resistive load. In this test, the chip generates a train of biphasic stimulation pulses at various output current levels of 100, 200, 500, and 1000  $\mu$ A. Each pulse is accurately modulated to produce a sinusoidal waveform with a  $5-\mu$ A ac amplitude. Fig. 9(b) shows the zoomed-in view of the pulse trains. The results indicate that the output at lower current levels is more accurate than higher current levels, i.e., the sinusoidal waveforms of 100 and 200  $\mu$ A are less distorted than 500 and 1000  $\mu$ A. This is again predicted in Fig. 2(b). Nevertheless, the waveform deviation at 1000- $\mu$ A level is still within a  $\pm 1 - \mu$ A accuracy.

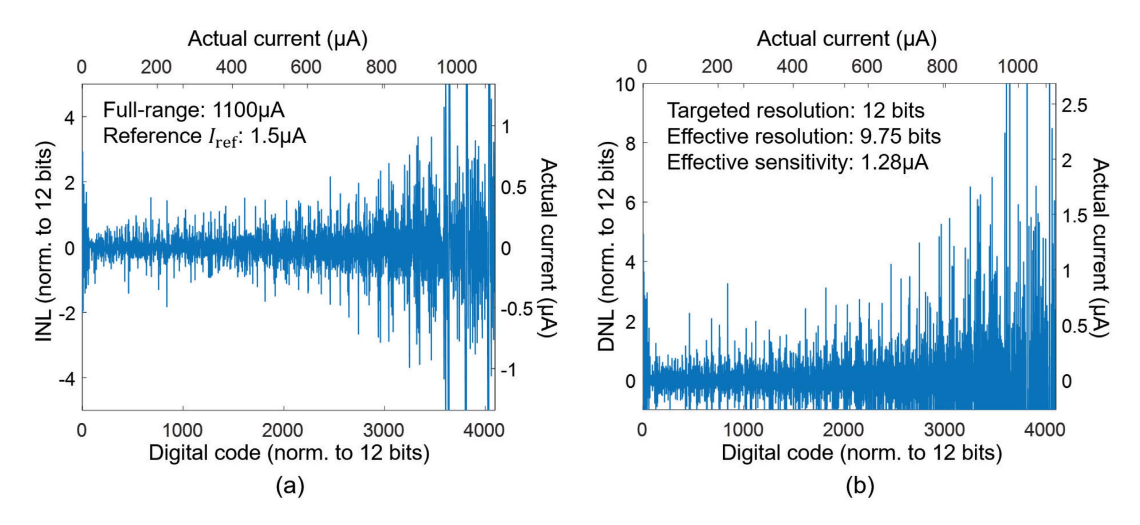


Fig. 8. Measured (a) INL and (b) DNL of a stimulator channel. Lower digital codes are more accurate because they are associated with more redundant configurations. Here, both the x-axis and y-axis are normalized to the targeted resolution 12 bits (upper bound) over the full range of 1.1 mA with a reference current  $I_{\text{ref}} = 1.5 \ \mu\text{A}$ .

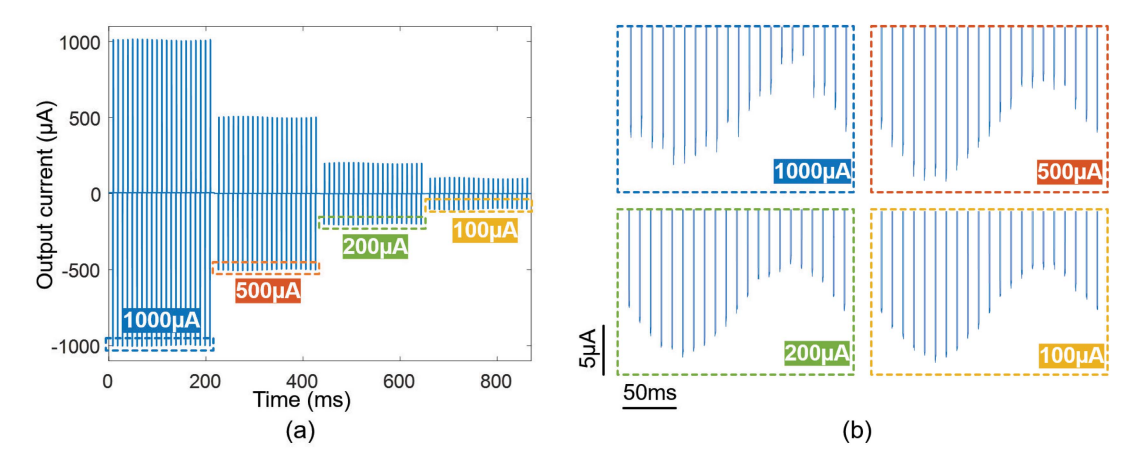


Fig. 9. (a) Train of biphasic stimulation pulses generated by the neurostimulator at various output current levels of 100, 200, 500, and 1000  $\mu$ A. Each pulse is accurately modulated to produce a sinusoidal waveform with a 5- $\mu$ A ac amplitude. (b) Zoomed-in view of the pulses showing a more accurate amplitude is achieved with a lower current level where there are more redundant configurations.

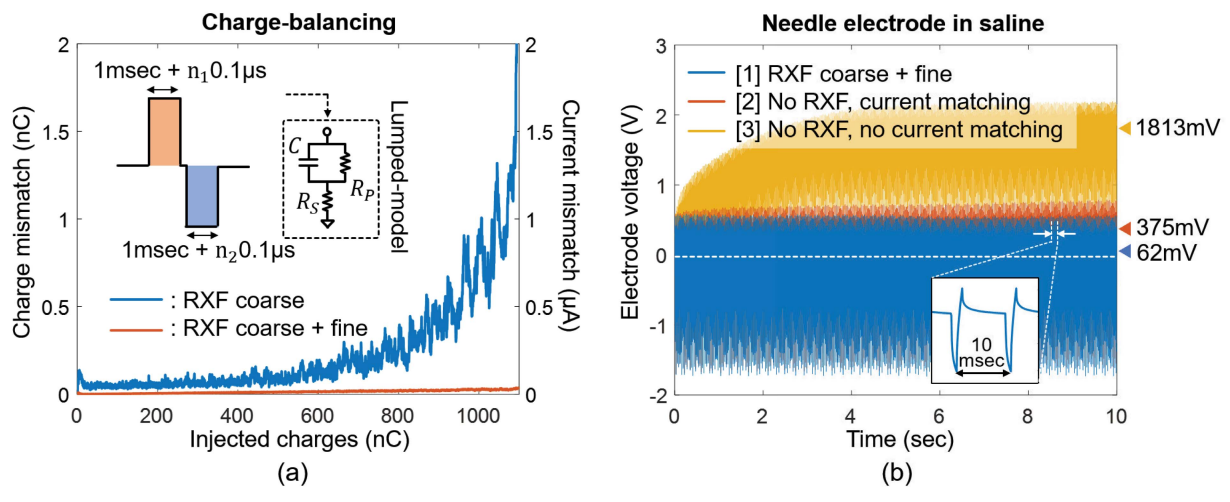


Fig. 10. (a) Measured charge-balancing characteristics where RXF coarse and fine calibration result in an insignificant charge mismatch across the output full range. (b) Rigorous benchmarking of charge balancing using needle electrodes in saline.

Fig. 10(a) shows the measured charge-balancing characteristics of a stimulator channel. We use 1-ms pulsewidth, anodic (positive) leading pulses, and a lumped electrode model

 $(C=0.5~\mu\text{F},~R_S=1~\text{k}\Omega,~\text{and}~R_P=10~\text{M}\Omega)$ . There are two levels of charge-balancing, coarse and fine, both of which are digitally calculated by the external controller based on the

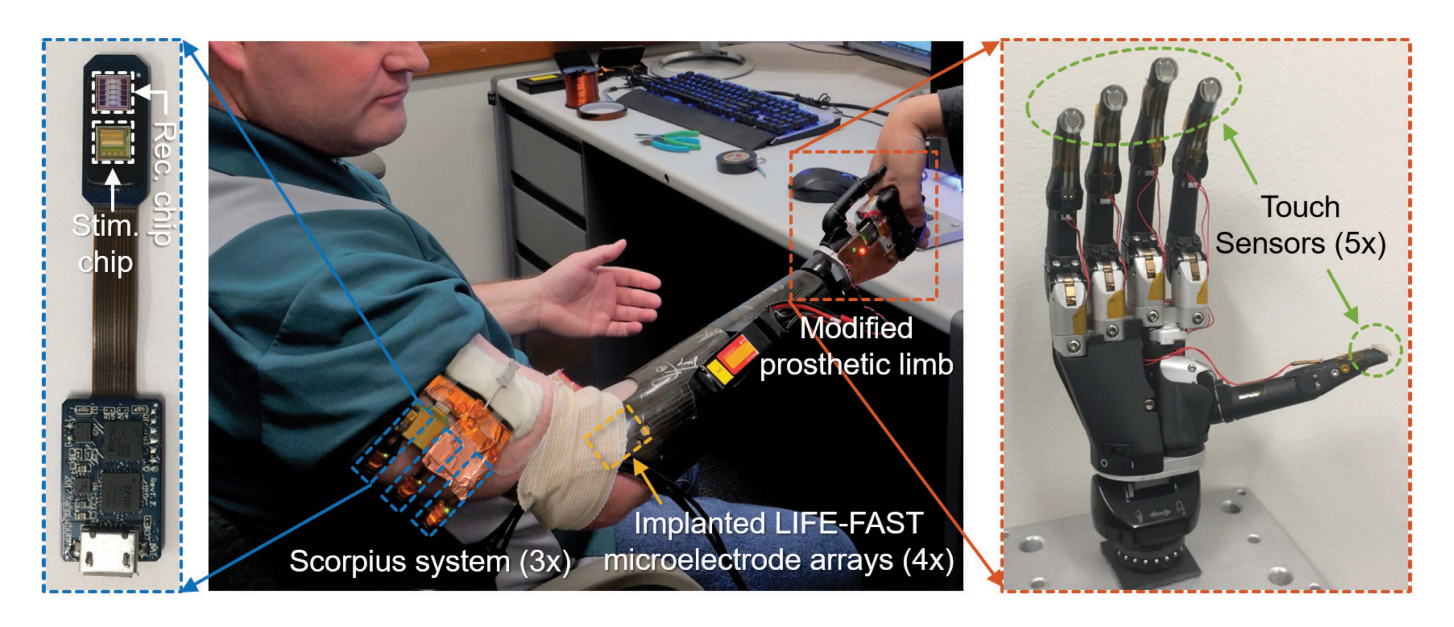


Fig. 11. Experiment setup for restoring somatosensation in a transradial amputee. The modified prosthetic hand is equipped with touch sensors at the fingertips. The sensor's read-out is used to modulate the current amplitude of the stimulation pulses in real time to create a continuous sense of touch.

measured currents and optimized configurations. The coarse calibration involves selecting the optimal IDAC and multiplier configuration of the second phase with current amplitude matching the first phase. This process is done during the one-time factory optimization based on the measured current of every RXF configuration. Both the IDAC and multiplier values are adjusted during the inter-phase delay and require less than  $10-\mu s$  settling time. The fine calibration involves digitally tuning the second phase's pulsewidth with  $0.1-\mu s$ step to further compensate for any residual mismatch between the absolute amplitudes of the anodic and cathodic currents. With coarse calibration alone, the current mismatch is less than 0.2% across the entire output full range. Again, lower current levels have more accurate matching. When combining fine calibration, the overall charge mismatch is reduced to an insignificant degree (<0.005%).

Fig. 10(b) shows an experiment to verify the stimulator's charge-balancing characteristics in saline. We use a pair of stainless-steel needle electrodes submerged in phosphate-buffered saline (PBS). The electrode's impedance is measured at 7.4 k $\Omega$  at 1 kHz. The stimulus is a train of cathodic leading, biphasic, symmetric pulses, 1-ms pulsewidth, and a targeted 200- $\mu$ A current amplitude. The stimulation rate is 100 Hz, which is the upper bound of our intended application. The 10-ms pulse-to-pulse spacing does not allow sufficient time for the electrode to discharge naturally. In the first measurement, where we use RXF with both coarse and fine calibration, after 1000 pulses, the electrode's residual voltage stabilizes at about 62 mV. The estimated current amplitudes are  $[-200.1, 200.0] \mu A$  and  $0.5 \mu s$  that are added to the second phase. In the second measurement, where we use only one multiplier (no RXF) but try to match the anodic and cathodic current with available configurations, the residual voltage reaches 375 mV and keeps increasing. The estimated current amplitudes are  $[-201.2, 201.6] \mu A$ . In the third

measurement, where we use neither RXF nor current matching, the residual voltage quickly reaches 1813 mV, saturating the electrode interface as water begins to be electrolyzed. The estimated current amplitudes are  $[-223.2, 230.7] \mu A$ .

## IV. NEUROPROSTHESIS APPLICATION

# A. Human Experiment Protocol

The human experiment protocol, including implantation surgery and nerve recording/stimulation procedures, are reviewed and approved by the Institutional Review Board (IRB) at the University of Minnesota (UMN) and the University of Texas Southwestern Medical Center (UTSW). The subject voluntarily participates in our study and is informed of the methods, aims, benefits, and potential risks. The implantation surgery is performed at the Clements University Hospital in the UTSW. The neuroprosthesis experiments are performed at UMN (Clinical trial identifier: NCT02994160).

# B. Experiment Setup

Fig. 11 shows a neuroprosthesis experiment to demonstrate the need for a high-resolution, fully integrated neurostimulator, which could be fulfilled by the proposed chip. The experiment is designed to restore somatosensation in a transradial amputee using electrical microstimulation while simultaneously acquiring nerve signals to control a prosthetic hand's movements. The neurostimulator chip is the essential part of the Scorpius neuromodulation system with both recording and stimulation functions. The design and specifications of the Scorpius system are reported in [32]. Three Scorpius devices are used in this setup, which can address 24 independent stimulation channels.

The patient is implanted with four longitudinal intrafascicular electrode (LIFE) arrays using the microsurgical fascicular targeting (FAST) technique. The FAST-LIFE microelectrodes

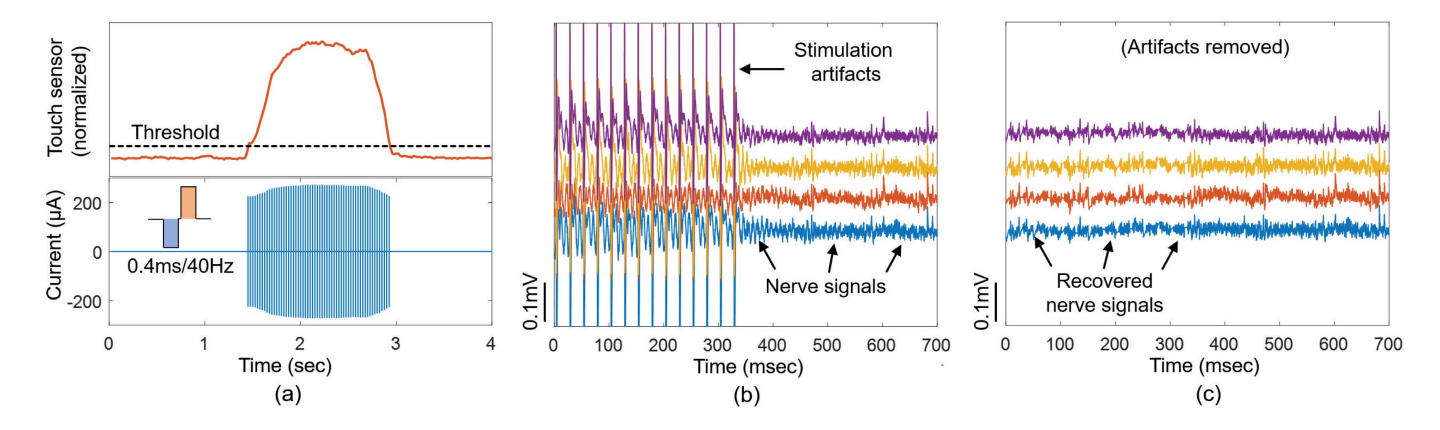


Fig. 12. (a) Sensor readouts and stimulation pattern as the prosthesis touches and releases an object. (b) Neural recordings from nearby electrodes show stimulation artifacts overlapped with nerve signals. (c) Artifacts can be removed to recover most of the nerve signals for motor decoding purposes.

target discrete fascicles in the median and ulnar nerves. The design and characteristics of the electrodes are reported in [33]. The electrode wires go through the patient's skin and connected to the Scorpius devices via standard Omnetics nano connectors.

The prosthesis is a heavily modified i-Limb Access hand (Touch Bionics, Livingston, U.K.). The hand is equipped with touch sensors (Interlink Electronics, CA, USA) at the fingertips. We replace the hand's driver with a customized controller using the ESP32-WROOM-32 module (Espressif Systems, Shanghai, China). The ESP32 samples force readouts from the sensors at 50 Hz and relays data to the host server via Bluetooth. The host server uses the sensor readouts to modulate the stimulation pulses' current amplitude to create various levels of touch sensation.

#### C. Results

Fig. 12(a) shows the stimulation pattern as the prosthesis touches and releases an object, which is applied to an electrode with clear sensory precepts from previous mapping experiments [33]. It is a train of cathodic leading, biphasic, symmetric pulses with a 0.4-ms pulsewidth, 40-Hz rate. The current amplitude is modulated to be proportional to the applied force. The pulses are only generated when the sensor readout is above a certain threshold.

The neurostimulator's super-resolution is essential for modulating the current amplitude with  $1-\mu A$  accuracy at any given threshold within a  $10-1100-\mu A$  range. In one particular electrode shown in Fig. 12(a), the current amplitude ranges from 220 to 280  $\mu A$ . The lower threshold 220  $\mu A$  is the smallest current amplitude that the patient can barely perceive sensation, while the higher threshold 280  $\mu A$  is the highest current amplitude that the patient can comfortably receive without experiencing pain. Thus, it is essential to produce an accurate current amplitude within this range to deliver continuous and desirable sensory feedback from light to strong touch. It is also worth noting that the current thresholds vary widely across electrodes, even for those within the same microelectrode array. The thresholds could be as low as  $15~\mu A$  and as high as  $1000~\mu A$ . However, for any specific

electrode, the "working" range (i.e., lower to higher threshold) is typically  $50-100 \mu A$ .

A charge-balanced neurostimulator also plays an important role in motor decoding experiments with simultaneous somatosensory feedback. Fig. 12(b) shows neural recordings acquired by the Scorpius system as the amputee flexes his phantom finger and stimulation is delivered to an adjacent electrode. The data show the stimulation artifacts overlapped with the nerve signals. Charge balancing helps reduce the impact of artifacts and prevent long-term charge accumulation, which could hinder the recorder's operation. Fig. 12(c) shows that the artifacts could be removed to recover most of the nerve data for decoding the amputee's motor intents. The artifacts are removed offline using the template matching method for demonstration purposes. A brief duration of 2–3 ms at the onset of each stimulation pulse is removed and replaced with a straight line because the recorder's input is fully saturated.

#### V. DISCUSSION AND FUTURE WORK

## A. Practical Considerations

The proposed technique only addresses static errors, i.e., errors that do not change over time or operating conditions. These errors include process variations and mismatches that alter the attributes of individual transistors during the fabrication process. The proposed technique does not compensate for dynamic errors, including thermal noise, kT/C noise, and temperature drift. For example, in this design, the reference current's noise floor would limit the circuit's effective resolution when pushing into nA range's sensitivity.

Temperature compensation could be needed if the design is intended for more general applications. As a low-power neurostimulator, the chip primarily operates at room and/or body temperature with a small thermal variation. Nevertheless, when testing the output at 90 °C using the calibration profile measured at room temperature, we observe an approximate 2.5% drifting of the output current, while the anodic and cathodic current amplitudes are still matched. This suggests the impact of operating temperature on the current reference, which is set by an external resistor. The issues may be

addressed in future implementation with an on-chip temperature sensor and compensation circuits.

## B. Circuit Optimization

A current multiplexer matrix could be implemented to allow one stimulator channel to support multiple nonconcurrent output electrodes. In the current implementation, a design decision was made to have one channel-one electrode so that the stimulation protocol is not restricted, allowing the stimulator to support a wider range of experiments. However, in certain applications where nonconcurrent outputs are permitted, having a multiplexer matrix could greatly increase the number of output channels and increase the area per channel density.

The chip area could be further optimized by moving parts of the circuits from high voltage (30 V) to low voltage (1.8 or 5 V). In the current implementation, a design decision was made to have the entire analog circuitry in high voltage and digital circuitry in low voltage, where the only interconnections between the high- and low-voltage sides are digital level shifters. Relocating blocks, such as the IDAC and current reference to the low-voltage domain, could reduce both chip area and static power consumption. However, extra safeguards and isolation are needed to ensure robust functionality.

Being fundamentally a CCS, the design does not offer a good energy efficiency compared to VCS and SCS. The difference between  $V_{\rm DD}/V_{\rm SS}$  and the electrode voltage results in wasted heat on the output driver. A well-known approach to improve efficiency is to implement a dynamic supply voltage scaling scheme [41], [42] where  $V_{\rm DD}/V_{\rm SS}$  are tuned to match the voltage drop on the electrode.

# VI. CONCLUSION

We present a new circuit technique called RXF to achieve super-resolution when designing a neurostimulator in ICs. Unlike previous methods, RXF exploits excessively large mismatch errors up to 10%–20% to boost the circuit's effective resolution. Both simulations and measurement results of the neurostimulator chip indicate a 10× performance boost due to the proposed method. Furthermore, RXF eliminates the concern on mismatch errors, which would help propel future designs into deep submicrometer processes. We show a proof-of-concept use of the high-resolution neurostimulator chip in a neuroprosthesis system to restore somatosensation. A similar design can be adopted in a wide range of neuromodulation applications where the stimulator is the essential component of a bidirectional human–machine interface.

## ACKNOWLEDGMENT

The authors are grateful for technical suggestions made by Hubert Lim, Bin He, Harvey Wiggins, Michael Park, and Wentai Liu. They are grateful to support from previous and current members at the Yang Lab at the University of Minnesota, including Tong Wu, Wing-kin Tam, Wenfeng Zhao, and Markus W. Drealan.

Z. Yang is a co-founder and holds equity in Fasikl Inc., a sponsor of this project. This interest has been reviewed and

managed by the University of Minnesota in accordance with its Conflict of Interest policy. J. Cheng and E. W. Keefer have ownership in Nerves Inc., a sponsor of this project.

#### REFERENCES

- S. K. Kelly *et al.*, "A hermetic wireless subretinal neurostimulator for vision prostheses," *IEEE Trans. Biomed. Eng.*, vol. 58, no. 11, pp. 3197–3205, Nov. 2011.
- [2] Y.-K. Lo, K. Chen, P. Gad, and W. Liu, "A fully-integrated high-compliance voltage SoC for epi-retinal and neural prostheses," *IEEE Trans. Biomed. Circuits Syst.*, vol. 7, no. 6, pp. 761–772, Dec. 2013.
- [3] N. Tran et al., "A complete 256-electrode retinal prosthesis chip," IEEE J. Solid-State Circuits, vol. 49, no. 3, pp. 751–765, Mar. 2014.
- [4] C.-L. Lee and C.-C. Hsieh, "A 0.8-V 4096-pixel CMOS Sense-and-Stimulus imager for retinal prosthesis," *IEEE Trans. Electron Devices*, vol. 60, no. 3, pp. 1162–1168, Mar. 2013.
- [5] E. Noorsal, K. Sooksood, H. Xu, R. Hornig, J. Becker, and M. Ortmanns, "A neural stimulator frontend with high-voltage compliance and programmable pulse shape for epiretinal implants," *IEEE J. Solid-State Circuits*, vol. 47, no. 1, pp. 244–256, Jan. 2012.
- [6] H. Ulusan, A. Muhtaroglu, and H. Kulah, "A sub-500 μW interface electronics for bionic ears," *IEEE Access*, vol. 7, pp. 132140–132152, 2019.
- [7] M. Yip, R. Jin, H. H. Nakajima, K. M. Stankovic, and A. P. Chandrakasan, "A fully-implantable cochlear implant SoC with piezoelectric middle-ear sensor and arbitrary waveform neural stimulation," *IEEE J. Solid-State Circuits*, vol. 50, no. 1, pp. 214–229, Jan. 2015.
- [8] J. A. George et al., "Biomimetic sensory feedback through peripheral nerve stimulation improves dexterous use of a bionic hand," Sci. Robot., vol. 4, no. 32, Jul. 2019, Art. no. eaax2352.
- [9] E. L. Graczyk, M. A. Schiefer, H. P. Saal, B. P. Delhaye, S. J. Bensmaia, and D. J. Tyler, "The neural basis of perceived intensity in natural and artificial touch," *Sci. Transl. Med.*, vol. 8, no. 362, 2016, Art. no. 362ra142.
- [10] C. M. Oddo et al., "Intraneural stimulation elicits discrimination of textural features by artificial fingertip in intact and amputee humans," eLife, vol. 5, Mar. 2016, Art. no. e09148.
- [11] M. Ortiz-Catalan, B. Håkansson, and R. Brånemark, "An osseointegrated human-machine gateway for long-term sensory feedback and motor control of artificial limbs," *Sci. Transl. Med.*, vol. 6, no. 257, Oct. 2014, Art. no. 257re6.
- [12] S. Raspopovic et al., "Restoring natural sensory feedback in real-time bidirectional hand prostheses," Sci. Transl. Med., vol. 6, no. 222, 2014, Art. no. 222ra19.
- [13] M. A. Schiefer, E. L. Graczyk, S. M. Sidik, D. W. Tan, and D. J. Tyler, "Artificial tactile and proprioceptive feedback improves performance and confidence on object identification tasks," *PLoS ONE*, vol. 13, no. 12, Dec. 2018, Art. no. e0207659.
- [14] D. W. Tan, M. A. Schiefer, M. W. Keith, J. R. Anderson, J. Tyler, and D. J. Tyler, "A neural interface provides long-term stable natural touch perception," *Sci. Transl. Med.*, vol. 6, no. 257, 2014, Art. no. 257ra138.
- [15] G. Valle et al., "Biomimetic intraneural sensory feedback enhances sensation naturalness, tactile sensitivity, and manual dexterity in a bidirectional prosthesis," *Neuron*, vol. 100, no. 1, pp. 37–45, Oct. 2018.
- [16] Y.-K. Lo et al., "A 176-channel 0.5 cm<sup>3</sup> 0.7g wireless implant for motor function recovery after spinal cord injury," in *IEEE Int.* Solid-State Circuits Conf. (ISSCC) Dig. Tech. Papers, Jan./Feb. 2016, pp. 382–383.
- [17] D. Rozgic et al., "A 0.338 cm<sup>3</sup>, artifact-free, 64-contact neuromodulation platform for simultaneous stimulation and sensing," *IEEE Trans. Biomed. Circuits Syst.*, vol. 13, no. 1, pp. 38–55, Feb. 2018.
- [18] B. Lee et al., "An implantable peripheral nerve recording and stimulation system for experiments on freely moving animal subjects," Sci. Rep., vol. 8, no. 1, p. 6115, Dec. 2018.
- [19] A. Zhou et al., "A wireless and artefact-free 128-channel neuromodulation device for closed-loop stimulation and recording in non-human primates," *Nature Biomed. Eng.*, vol. 3, no. 1, pp. 15–26, 2019.
- [20] W.-M. Chen et al., "A fully integrated 8-channel closed-loop neural-prosthetic CMOS SoC for real-time epileptic seizure control," IEEE J. Solid-State Circuits, vol. 49, no. 1, pp. 232–247, Jan. 2014.

- [21] A. T. Nguyen, J. Xu, W.-K. Tam, W. Zhao, T. Wu, and Z. Yang, "A programmable fully-integrated microstimulator for neural implants and instrumentation," in *Proc. IEEE Biomed. Circuits Syst. Conf. (BioCAS)*, Shanghai, China, Oct. 2016, pp. 472–475.
- [22] J. Xu, H. Guo, A. Nguyen, H. Lim, and Z. Yang, "A bidirectional neuromodulation technology for nerve recording and stimulation," *Micromachines*, vol. 9, no. 11, p. 538, Oct. 2018.
- [23] B. Lee et al., "An inductively-powered wireless neural recording and stimulation system for freely-behaving animals," IEEE Trans. Biomed. Circuits Syst., vol. 13, no. 2, pp. 413–424, Apr. 2019.
- [24] P. G. Drennan and C. C. McAndrew, "Understanding MOSFET mismatch for analog design," *IEEE J. Solid-State Circuits*, vol. 38, no. 3, pp. 450–456, Mar. 2003.
- [25] P. R. Kinget, "Device mismatch and tradeoffs in the design of analog circuits," *IEEE J. Solid-State Circuits*, vol. 40, no. 6, pp. 1212–1224, Jun. 2005.
- [26] P. D. Aluthwala, N. Weste, A. Adams, T. Lehmann, and S. Parameswaran, "Partial dynamic element matching technique for digital-to-analog converters used for digital harmonic-cancelling sine-wave synthesis," *IEEE Trans. Circuits Syst. I, Reg. Papers*, vol. 64, no. 2, pp. 296–309, Feb. 2017.
- [27] X. Yuan et al., "Transistor mismatch properties in deep-submicrometer CMOS technologies," *IEEE Trans. Electron Devices*, vol. 58, no. 2, pp. 335–342, Feb. 2011.
- [28] A. T. Nguyen, J. Xu, and Z. Yang, "A bio-inspired redundant sensing architecture," in *Proc. Neural Inf. Process. Syst. (NIPS)*, Barcelona, Spain: Curran Associates, 2016, pp. 2379–2387.
- [29] A. T. Nguyen, J. Xu, D. K. Luu, Q. Zhao, and Z. Yang, "Advancing system performance with redundancy: From biological to artificial designs," *Neural Comput.*, vol. 31, no. 3, pp. 555–573, Mar. 2019.
- [30] D. K. Luu, A. T. Nguyen, and Z. Yang, "Achieving super-resolution with redundant sensing," *IEEE Trans. Biomed. Eng.*, vol. 66, no. 8, pp. 2200–2209, Aug. 2019.
- [31] A. T. Nguyen, J. Xu, and Z. Yang, "A 14-bit 0.17 mm<sup>2</sup> SAR ADC in 0.13μm CMOS for high precision nerve recording," in *Proc. IEEE Custom Integr. Circuits Conf. (CICC)*, San Jose, CA, USA, Sep. 2015, pp. 1–4.
- [32] A. T. Nguyen et al., "A bioelectric neural interface towards intuitive prosthetic control for amputees," J. Neural Eng., vol. 17, no. 6, Nov. 2020, Art. no. 066001.
- [33] C. K. Overstreet, J. Cheng, and E. W. Keefer, "Fascicle specific targeting for selective peripheral nerve stimulation," *J. Neural Eng.*, vol. 16, no. 6, Nov. 2019, Art. no. 066040.
- [34] P. Harpe, H. Hans, and A. van Roermund, Smart AD and DA Conversion. Dordrecht, The Netherlands: Springer, 2010.
- [35] H.-M. Lee, H. Park, and M. Ghovanloo, "A power-efficient wireless system with adaptive supply control for deep brain stimulation," *IEEE J. Solid-State Circuits*, vol. 48, no. 9, pp. 2203–2216, Sep. 2013.
- [36] H.-M. Lee, K. Y. Kwon, W. Li, B. Howell, W. M. Grill, and M. Ghovanloo, "A power-efficient switched-capacitor stimulating system for electrical/optical deep brain stimulation," *IEEE J. Solid-State Circuits*, vol. 50, no. 7, pp. 360–374, Jan. 2015.
- [37] H.-M. Lee, B. Howell, W. M. Grill, and M. Ghovanloo, "Stimulation efficiency with decaying exponential waveforms in a wirelessly powered switched-capacitor discharge stimulation system," *IEEE Trans. Biomed. Eng.*, vol. 65, no. 5, pp. 1095–1106, May 2018.
- [38] F. Shahrokhi, K. Abdelhalim, D. Serletis, P. L. Carlen, and R. Genov, "The 128-channel fully differential digital integrated neural recording and stimulation interface," *IEEE Trans. Biomed. Circuits Syst.*, vol. 4, no. 3, pp. 149–161, Jun. 2010.
- [39] S. K. Arfin and R. Sarpeshkar, "An energy-efficient, adiabatic electrode stimulator with inductive energy recycling and feedback current regulation," *IEEE Trans. Biomed. Circuits Syst.*, vol. 6, no. 1, pp. 1–14, Feb. 2012.
- [40] K.-H. Chang and C.-C. Hsieh, "A hybrid analog-to-digital conversion algorithm with sub-radix and multiple quantization thresholds," *IEEE Trans. Circuits Syst. I, Reg. Papers*, vol. 64, no. 6, pp. 1400–1408, Jun. 2017.
- [41] I. Williams and T. G. Constandinou, "An energy-efficient, dynamic voltage scaling neural stimulator for a proprioceptive prosthesis," *IEEE Trans. Biomed. Circuits Syst.*, vol. 7, no. 2, pp. 129–139, Apr. 2013.
- [42] A. Rashidi, N. Yazdani, and A. M. Sodagar, "Fully-implantable, multichannel, microstimulator with tracking supply ribbon and energy recovery," in *Proc. 38th Annu. Int. Conf. IEEE Eng. Med. Biol. Soc. (EMBC)*, Aug. 2016, pp. 1818–1821.



Anh Tuan Nguyen (Member, IEEE) received the B.Eng. degree in electrical engineering with specialization in analog and mixed-signal integrated circuit design from the National University of Singapore, Singapore, in 2014, and the Ph.D. degree in biomedical engineering from the University of Minnesota, Minneapolis, MN, USA, in 2021.

From 2012 to 2016, he was an Undergraduate Research Assistant and a Research Engineer with the Department of Electrical and Computer Engineering and the Interactive and Digital Media Institute,

National University of Singapore, Singapore. He is currently a Post-Doctoral Associate with the Department of Biomedical Engineering, University of Minnesota, and a Consultant for Fasikl Inc., Minneapolis. His research interests include human–machine symbiosis, fully integrated bioelectronics, bidirectional neural interface, dexterous and intuitive neuroprosthesis, machine learning, and artificial intelligence.



**Jian Xu** (Member, IEEE) received the B.S. and Ph.D. degrees from Zhejiang University, Hangzhou, China, in 2007 and 2012, respectively.

From March 2011 to July 2012, he was a Visiting Scholar and Research Engineer with the Department of Electrical and Computer Engineering, National University of Singapore, Singapore, where he also worked as a Research Fellow and Senior Research Fellow from 2012 to 2016. From 2016 to 2020, he was a Researcher with the Department of Biomedical Engineering, University of Minnesota, Min-

neapolis, MN, USA. His research interests include brain-computer interface and brain neuromodulation, bioelectronics therapies for neurological diseases, neural signal processing, implantable/wearable medical devices, and biomedical circuits.



**Diu Khue Luu** received the B.S. degree in economics from the National University of Singapore, Singapore, in 2015. She graduated with the First Class Honors and a GPA among the top 5% of her class. She is currently pursuing the Ph.D. degree in biomedical engineering (GPA: 4.0/4.0) with the University of Minnesota, Minneapolis, MN, USA.

She helped develop a mathematical framework to achieve super-resolution in analog-to-digital and digital-to-analog converters. She is currently studying the deployment of machine learning techniques

with an emphasis on deep learning to enable bidirectional communication between the peripheral nervous system and computers. She hopes to contribute to developing a fully implantable system to enable intuitive control of sensory feedback from hand prostheses to improve amputees' well-being. Her research focuses on the application of advanced computational techniques in designing biomedical devices and systems.



**Cynthia K. Overstreet** received the B.S.E. degree in biomedical engineering with an emphasis on bioelectricity from Case Western Reserve University, Cleveland, OH, USA, in 2008, and the Ph.D. degree in biomedical engineering from Arizona State University, Tempe, AZ, USA, in 2013.

Her research focuses on selective electrical stimulation of the central and peripheral nervous systems, particularly as applied to neuroprosthetic devices. Her work has included psychophysical studies of sensation and perception, experimental studies with

human subjects, and computational modeling of electrical stimulation in neural tissue



Jonathan Cheng received the B.A. degree in chemical physics from Rice University, Houston, TX, USA, in 1996, and the M.D. degree from the Baylor College of Medicine, Houston, in 2000. He completed a residency in plastic surgery at the Medical College of Wisconsin, Milwaukee, WI, USA, in 2006, and received advanced training in hand, microvascular, and peripheral nerve surgery through a fellowship at Barnes-Jewish Hospital, Washington University Medical Center, Saint Louis, MO, USA, in 2007. As the Kroll Memorial Scholarship Recip-

ient, he received further specialized training in perforator flap and breast reconstructive microsurgery at University Hospital Ghent, Ghent, Belgium.

He is currently a Professor, the Chief of Pediatric Hand, Peripheral Nerve, and Microvascular Surgery, and the Director of the Basic and Translational Research Nerve Laboratory, Department of Plastic Surgery, University of Texas Southwestern Medical Center, Dallas, TX, USA. His research focuses on basic mechanisms of long gap nerve regeneration and on the science and clinical applications of integrating prosthetics in amputees to provide both motor control and sensory input via microsurgical integration of prosthetics and the peripheral nervous systems.



**Edward W. Keefer** received the M.S. and Ph.D. degrees from the Laboratory of Guenter Gross, University of North Texas, Denton, TX, USA, a pioneer of *in vitro* multielectrode recording, in 1998 and 2001, respectively.

He was with Nobel Laureate Gerald Edelman, Neurosciences Institute, San Diego, CA, USA, where he acquired expertise in molecular biology, neuronal cell biology, and behavioral electrophysiology and was the first to show that stem cell-derived neural networks can elicit spontaneous activity.

He has been focusing on peripheral nerve electrode interfaces for the control of prosthetic devices since 2006 and is a pioneer in using carbon nanotubes to improve neural electrodes. He is currently a Chief Executive Officer of Nerves Inc., Dallas, TX, USA. He has authored extensively on the use of neuronal networks for pharmacology and toxicology assays. His research interests include the development of nanotechnology, advanced materials, and novel recording techniques for brain/machine interfaces, advancing nerve regeneration through the understanding of molecular and cell biology.



**Zhi Yang** (Member, IEEE) received the B.S. degree from Zhejiang University, Hangzhou, China, in 2004, and the M.S. and Ph.D. degrees from the University of California, Santa Cruz, CA, USA, in 2007 and 2010, respectively.

He was an Assistant Professor with the Department of Electrical and Computer Engineering, National University of Singapore, Singapore, from 2010 to 2015. He is currently an Associate Professor of biomedical engineering with the University of Minnesota, Minneapolis, MN, USA, where he is

also with the MnDRIVE Robotics Program. Since 2015, he has been with the Department of Biomedical Engineering, University of Minnesota. He has directed 15 funded research projects from federal agencies in the U.S. and Singapore. He has coauthored 80 publications on bioelectronics and signal processing and edited one book titled *Neural Computation, Neural Device*, and *Neural Prosthesis*. His research interests include neural recording and stimulation devices, bidirectional neural communication, and neural signal processing.

Dr. Yang was a recipient of the Best Paper Honorable Mention at ACCV 2009, the Singapore Young Investigator Award 2012, the regional MIT TR35 2014, and the NSF CAREER Award 2019. He co-founded Fasikl in 2019 and works as the President to innovate AI-enabled neuromodulation therapies.